# Remote Plasma Physics Research and Teaching by Example of Turbulence Study at the University-Scale Tokamak GOLEM

G. Sarancha, Ya. Ammosov, A. Balashov, N. Butrova, O. Krokhalev, A. Loginov, A. Melnikov, M. Popova, A. Stepin, A. Stolbov, V. Svoboda, S. Suntsov, G. Timkovskiy & GOLEM Team

Published online: 10 Feb 2023.

Submit your article to this journal ⬈

View related articles ⬈

View Crossmark data ⬈

⊗ANS®

[Check for updates]

# Remote Plasma Physics Research and Teaching by Example of Turbulence Study at the University-Scale Tokamak GOLEM

G. Sarancha,[a,b]* Ya. Ammosov,[a,b,c] A. Balashov,[a] N. Butrova,[d] O. Krokhalev,[a,b] A. Loginov,[b] A. Melnikov,[a,b,d] M. Popova,[c] A. Stepin,[a] A. Stolbov,[d] V. Svoboda,[e] S. Suntsov,[a,d] G. Timkovskiy,[d] and GOLEM Team[e]

[a]*National Research Center "Kurchatov Institute," Moscow, Russia*
[b]*Moscow Institute of Physics and Technology (National Research University), Dolgoprudny, Russia*
[c]*RUDN University, Moscow, Russia*
[d]*National Research Nuclear University MEPhI, Moscow, Russia*
[e]*Czech Technical University in Prague, Prague, Czech Republic*

**Abstract** — *The university-scale tokamak GOLEM provides a unique opportunity to perform remote thermonuclear experiments [V. Svoboda, J. Fusion Energy, Vol. 38, Part 2, p. 253 (2019)]. Undergraduate plasma physics students from three universities—Moscow Institute of Physics and Technology (National Research University), RUDN University, and National Research Nuclear University MEPhI—carried out joint remote experiments to train in tokamak operation and to study topics relevant for mainstream fusion research such as plasma start-up, comparison of hydrogen versus helium plasma characteristics, electrostatic and electromagnetic turbulence, long-range correlations, etc. New observations of the long-range correlations between low-frequency (<50 kHz) quasi-coherent electrostatic and magnetic oscillations identified as m = 2 mode with several techniques were done, as well as of the broadband (<250 kHz) magnetic oscillations resolved in frequency and wave vector in helium and hydrogen plasmas. The presence of broadband electrostatic and broadband magnetic turbulence has also been established at the plasma edge.*

**Keywords** — *Tokamak, GOLEM, magnetohydrodynamics, electrostatic and magnetic turbulence, long-range correlations.*

**Note** — *Some figures may be in color only in the electronic version.*

## I. INTRODUCTION

Nowadays, physics has reached a level of mega-science devices like the Large Hadron Collider, European Center for Synchrotron Radiation, International Thermonuclear Experimental Reactor (ITER), etc. Large-scale experimental sessions take months to plan, and their realization takes multiple years, which are periods of time that do not necessarily align with the university education period. So, it is difficult for a young generation of experimentalists to get practical training and impossible for them to perform their own experiment plan.

The life cycle of a large thermonuclear device from its conception to operation typically exceeds a decade, like in the case of Wendelstein-7X, the world's largest stellarator, and it may even take several decades, like in the case of ITER. During this time, the team that starts its creation and partially or even completely manages it may change by the time of the operation stage. In this case, there may be many newcomers that have never participated in a plasma experiment in their lives. Because of this, they may not get a chance to work directly with any plasma device for years. The university-scale tokamak GOLEM is used as a test bench for young plasma physicists to make their first experiments by themselves, to

*E-mail: sarancha.ga@phystech.edu

feel a spirit of the modern experimental work, and to derive satisfaction by obtaining their own first results. During the university course, students have an opportunity not only to understand the basic principles of tokamak operation but also to immerse themselves in the intricacies of high-temperature plasma diagnostics and data processing and to study modern plasma physics directly.

In contrast to the standard university laboratory work in physics with known physical processes and known solution, the GOLEM experiments are dedicated to open questions of modern plasma physics research with the teacher acting not as a lecturer and mentor but as an elder colleague. Thanks to such an organization of education, the thermonuclear community will have a continuous stream of qualified personnel who are ready to start working with a large thermonuclear device without a long acquainting period.

For the students, in the experiment the key elements are to prepare a list of tasks, relevant for mainstream fusion research, and to equip the machine with adequate diagnostic and technology systems. The approaches to get such synergy and the results obtained are the topic of this paper.

GOLEM is a small tokamak operating at the Faculty of Nuclear Sciences and Physical Engineering, Czech Technical University in Prague, Czech Republic. It was manufactured in 1966 and operated in the Soviet Union in the Kurchatov Institute, the birthplace of tokamaks until 1983 under the name TM-1, later TM-1-MH. Then, it was donated to the Czechoslovak Academy of Sciences and transferred to the Institute of Plasma Physics in Prague, where it worked under the name CASTOR for almost 30 years. Since 2009, it got the name GOLEM and started to be a platform for research work of students from the Faculty of Nuclear Sciences and Physical Engineering and also from abroad. GOLEM is an ohmically heated circular tokamak, equipped with basic diagnostics, and it provides experiments in various areas relevant for basic plasma physics and mainstream fusion research[1,2] with access all over the world via Web interface.[3–5] For instance, helium plasma is quite unique in operating fusion machines. It is mostly studied on large-scale devices and dedicated to ITER-relevant studies for its starting nonnuclear operation stage. Helium plasma performance is always lower than hydrogen or deuterium performance with identical plasma current $I_{pl}$, toroidal magnetic field $B_t$, line-averaged electron density $\overline{n_e}$, and heating power.[6] It contradicts the isotope effect suggesting better confinement for the species with larger mass. Theoretical mechanisms including $E \times B$ shearing[7,8] and collisional effects[9] were proposed to explain this effect, but for the moment there is no explanation.

The study of energy and particle transport across the confining magnetic field of a toroidal device—a tokamak or a stellarator—is one of the main problems of modern high-temperature plasma physics. Experiments show that plasma transport significantly exceeds the predictions of neoclassical theory, being anomalous, associated with plasma turbulence. Multiscale turbulence presents the dynamical combination of eddies with various time and space scales, from the electron Larmor radius up to the global poloidally and toroidally symmetric zonal flows ($n = m = 0$) (Refs. 10 through 13) and their high-frequency counterpart Geodesic Acoustic Mode, observed in various machines[14–17] including STOR-M (Ref. 18), comparable to GOLEM. These global modes manifest themselves by long-range toroidal correlations (LRC) and poloidal correlations of plasma potential.[19–21]

The paper is organized as follows. Section II is dedicated to the machine description and the experimental setup, including the methods of the experimental data processing. Section III presents the analysis of magnetic signals and magnetohydrodynamic (MHD) modes. Section IV shows the broadband magnetic turbulence. Section V discusses LRC.

## II. EXPERIMENTAL SETUP

During the remote experiment, it is possible to prepare the vacuum vessel, to set the required discharge parameters, to conduct an experiment, and to collect diagnostic data via the internet by prior agreement with the machine manager. The GOLEM tokamak has a limiter configuration; the main plasma parameters are presented in Table I.

### II.A. Diagnostics Setup

The diagnostic complex (Fig. 1) consists of the following:

1. Two toroidally separated arrays of 4 and 16 magnetic probes [Mirnov coils (MCs)].

2. Rogowskii coil.

3. Langmuir probe (LP), located at the bottom of the vacuum chamber.

4. Double rake probe (DRP), located at the bottom.

Magnetic perturbations are studied by magnetic probes. They are located in two vertical cross sections very close to the plasma edge at the radius $r_{MC}$=9.35 cm; see Fig. 2. The letter "L" in the name of the magnetic probe marks the set of MCs placed at the limiter cross

TABLE I

Parameters of the GOLEM Tokamak

| | |
|---|---|
| Major radius, $R$ (cm) | 40 |
| Minor radius, $a$ (cm) | 10 |
| Limiter radius, $a_{lim}$ (cm) | 8.5 |
| Toroidal magnetic field, $B_t$ (T) | <0.8 |
| Plasma current, $I_{pl}$ (kA) | <10 |
| Electron temperature, $T_{0e}$ (eV) | <100 |
| Plasma density, $n_{0e}$ (cm$^{-3}$) | <$10^{12}$ |
| Working gas | H/He |
| Discharge duration, $\tau$ (ms) | <20 |
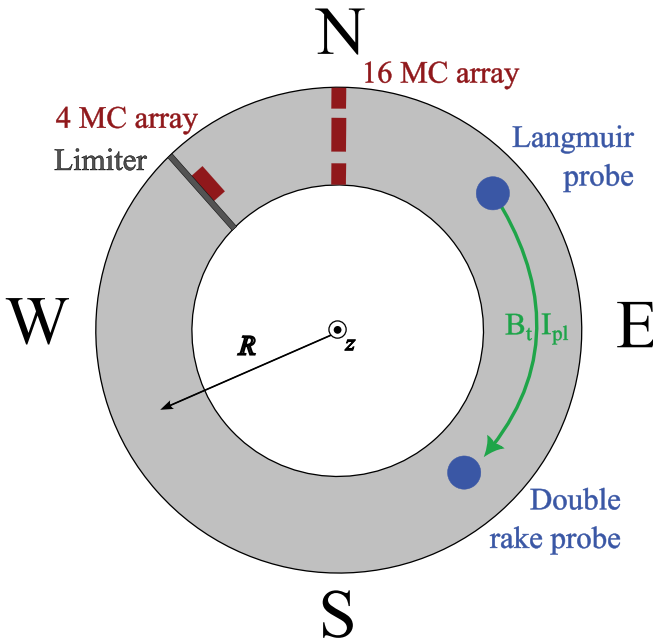


Fig. 1. Setup of GOLEM diagnostics. View from the top of the tokamak.

section as shown in Fig. 2b. Analysis of the MC signals allows one to reconstruct the mode structure of magnetic field perturbation.

In addition, analysis allows one to determine the positions $\Delta r$ and $\Delta z$ and the radius $a_{pl}$ of the plasma column. Poloidal magnetic field $B$ can be calculated by the law of electromagnetic induction:

$$B(t) = -\frac{1}{\langle NS \rangle} \int_0^t U(\tau)d\tau \ , \qquad (1)$$

where $\langle NS \rangle = 38$ cm$^2$ is the effective area of each MC. The measured $B$ by four MCs allows us to determine the plasma position with respect to the minor axis of the torus[22] in the horizontal and vertical directions; see Fig. 2b:

$$\Delta r = \frac{B_{\text{MC}-1\text{L}} - B_{\text{MC}-9\text{L}}}{B_{\text{MC}-1\text{L}} + B_{\text{MC}-9\text{L}}} \cdot r_{\text{MC}} \ , \qquad (2)$$

and

$$\Delta z = \frac{B_{\text{MC}-5\text{L}} - B_{\text{MC}-13\text{L}}}{B_{\text{MC}-5\text{L}} + B_{\text{MC}-13\text{L}}} \cdot r_{\text{MC}} \ . \qquad (3)$$

Since the plasma column is limited by the circular limiter, the current plasma radius is

$$a_{pl}(t) = a_{lim} - \sqrt{(\Delta r(t))^2 + (\Delta z(t))^2} \ . \qquad (4)$$

The setup of the LP and the DRP is presented in Fig. 3.

## II.B. Discharge Scenario

Experiments were carried out in hydrogen plasma with line-averaged density $\overline{n_e} \approx 0.8 \times 10^{12}$ cm$^{-3}$. The machine power supply does not allow one to get the stationary value of $B_t$, so the discharge takes place in an increasing magnetic field. The discharge scenario is shown in Fig. 4. It can be divided into three stages:

*Stage I*: Breakdown and the initial stage of the discharge (3 to 5 ms). There is a quasi-linear $I_{pl}$ increase and a significant drop of loop voltage $U_{loop}$ (from 10 to 6 V). This stage is characterized by a current up to 1.5 kA.

*Stage II*: The gradual rise of $I_{pl}$ and $U_{loop}$ up to a plateau (5 to 11 ms) is accompanied by small-scale fluctuations in the plasma current and loop voltage.

*Stage III*: The final phase of the discharge (11 to 14 ms) is characterized by a decrease in $I_{pl}$ and an increase in $U_{loop}$, leading to the discharge end, and is accompanied by a noticeable decrease in the plasma minor radius.

Figures 5a and 5b show the evolution of the plasma position during the discharge. The plasma column
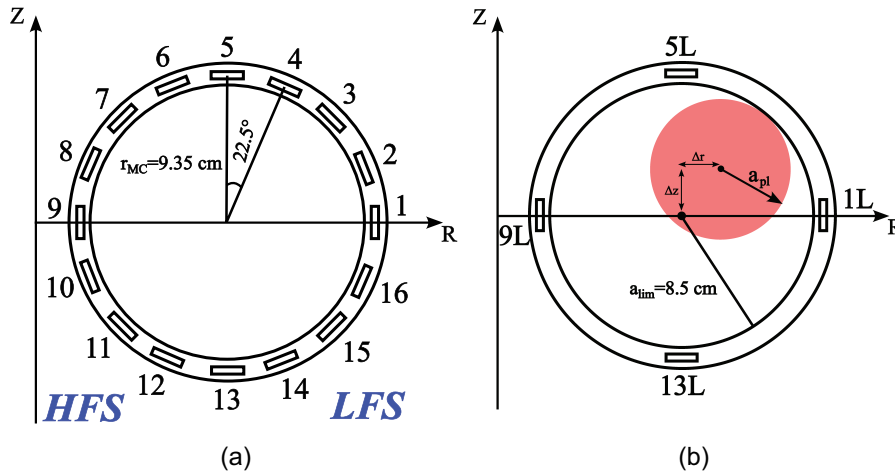
⊗ANS

Fig. 2. Poloidal cross sections with MC arrays: (a) 16 MCs and (b) MC-5L, MC-1L, MC-13L, and MC-13L, where "L" marks the four MCs, located at the limiter cross section. HFS = high-field side of the machine; LFS = low-field side of the machine. Red circle denotes an example of the plasma column position.
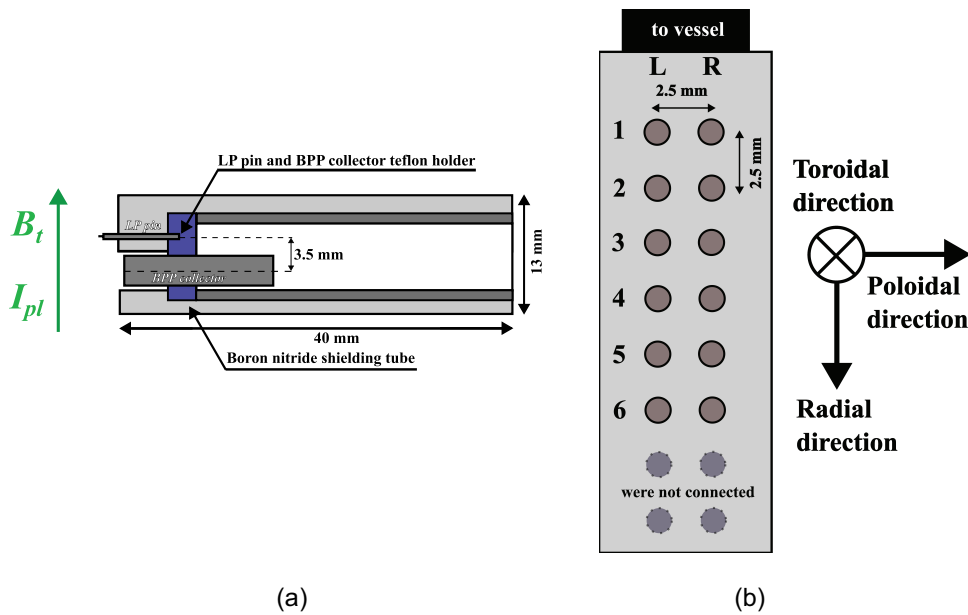


Fig. 3. Scheme of (a) Langmuir and ball-pen probes and (b) double rake probe.

initially moves outward to the high-field side (LFS) and slightly upward, and finally, it moves toward the high-field side (HFS).

## II.C. Data Processing for Correlation Studies

The Fourier correlation method is used to search for the links between measured fluctuating quantities.[23] For Fourier images $\mathcal{F}_x(f,t)$ and $\mathcal{F}_y(f,t)$ for the experimental discrete signals $x(t_n)$ and $y(t_n)$, the power spectral density (PSD) of the oscillations is determined as

$$\mathrm{PSD}_{xx} = \mathcal{F}_x(f,t)\mathcal{F}_x^*(f,t) \quad , \tag{5}$$

the power cross-spectral density (CSD) is determined as

$$\mathrm{CSD}_{xy} = \mathcal{F}_x(f,t)\mathcal{F}_y^*(f,t) \quad , \tag{6}$$

the quadratic coherence coefficient $\gamma^2$ (hereinafter called the coherence coefficient) is determined as

$$0 \leq \gamma^2(f,t) = \frac{\langle \mathrm{CSD}_{xy} \rangle^2}{\langle \mathrm{PSD}_{xx} \rangle \langle \mathrm{PSD}_{yy} \rangle} \leq 1 \quad , \tag{7}$$
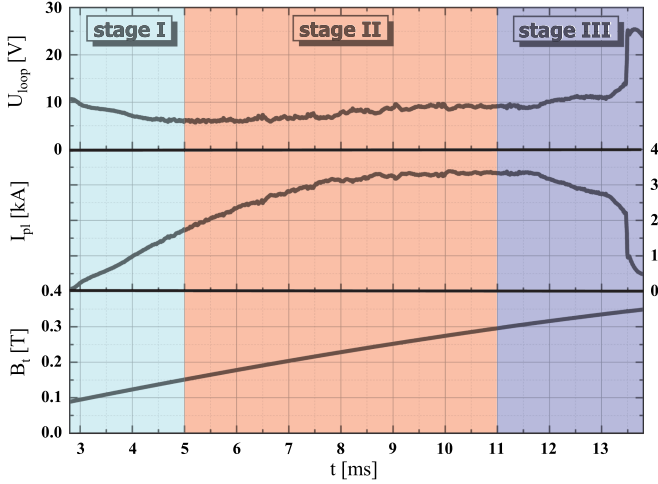
Fig. 4. Time traces of loop voltage $U_{loop}$, plasma current $I_{pl}$, and toroidal magnetic field $B_t$ during typical plasma discharge #36598.

and the cross phase is determined as

$$-\pi < \Delta\theta = \text{arctg}\frac{\text{Im}(\text{CSD}_{xy})}{\text{Re}(\text{CSD}_{xy})} \leq \pi \quad , \tag{8}$$

where $^*$ denotes complex conjugation; $\langle\rangle$ is time averaging over windows; and Im and Re are the imaginary and real parts of the complex number, respectively. The parameters of multi-window fast Fourier transform ensemble length $N_{FFT} = 256$ and window length $N_{Window} = 64$ for Eqs. (5) through (8) are chosen constant. The half-window overlapping gives $n = 2\frac{N_{FFT}}{N_{Window}} - 1 = 7$ windows per ensemble (Fig. 6).

Confidence level $\gamma_{conf}^2$ for the coherence coefficient is defined as[24]

$$\gamma_{conf}^2 = 1 - \alpha^{\frac{1}{n-1}} = 0.33 \quad , \tag{9}$$

where $\alpha = 1 - 0.95 = 0.05$. For Eqs. (7) and (8), a longer ensemble is reasonable to reduce the $\gamma_{conf}^2$ estimation: $\gamma_{conf}^2 = 0.19$ for $N_{FFT} = 512$. The experimentally estimated coherence noise level averaged over the whole discharge stage is 0.15.

## III. MAGNETIC ACTIVITY STUDY

Magnetic oscillations were studied in each stage of the discharge. On the cross-power spectrograms of magnetic oscillations, there are no significant fluctuations observed in the first stage, while in the second stage of the discharge, the dominant frequency of $50 \pm 20$ kHz is pronounced; see Fig. 7. The third stage is characterized by an additional peak

at 20 kHz at the top and at the HFS magnetic probes, which are closest to the plasma location.

Figure 7 shows that magnetic turbulence exhibits a broadband ($f < 250$ kHz) component that supports the earlier observation in helium discharges.[25] In addition, in the hydrogen discharges under study, a quasi-coherent component with the peak frequency $f \sim 50$ kHz occurs.

To analyze the poloidal structure of turbulence, the technique for constructing coherence matrices was applied; see Table II. The row and column numbers correspond to the channel numbers (16 Mirov probes). In the matrix cells, the coherence coefficient $\gamma_{ij}^2$ between channels $i$ and $j$ averaged over the stage duration and three frequency ranges ($20 \pm 10$, $50 \pm 20$, and $150 \pm 30$ kHz) is plotted. Channels are numbered from left to right and from bottom to top. It can be seen that during the discharge, the most coherent magnetic oscillations take place at the LFS in the frequency range up to 70 kHz. When comparing the first and second stages of the discharge, an increase in the coherence length for low-frequency oscillations (20 kHz) and medium-frequency oscillations (50 kHz) in a clockwise direction (i.e., HFS-up) is observed. At the same time, high-frequency oscillations (over 150 kHz) demonstrate the opposite trend: The HFS-bottom coherence increases while the HFS-top coherence remains unchanged.

The time-channel contour plot of magnetic probe signal oscillations (see Fig. 8) shows a mode with a poloidal mode number $m = 2$ rotating in the direction of LFS-bottom–HFS-top at a frequency of 50 kHz. It is noteworthy that the line has a steeper slope at the HFS, indicating the faster propagation of the perturbation.

To analyze the poloidal mode structure, the technique of the cross-phase matrices[26] was applied for the 50-kHz mode with $m = 2$; see Fig. 9. The cross-phase matrix is built similarly to the coherence matrix; however, the values in the cells are the cross phase between the signals of the magnetic probes, averaged over a time interval of 0.5 ms and a frequency range of 30 to 70 kHz. Figure 8 independently confirms $m = 2$. A deformation of the diagonal structure for 9 ms is caused by displacement of the plasma column upward and outward. When modeling the matrix of cross phases for the $m = 2$ mode, the so-called Merezhkin transform[27,28] is used:

$$\vartheta^* = \vartheta - \lambda \sin\vartheta \quad , \tag{10}$$

where

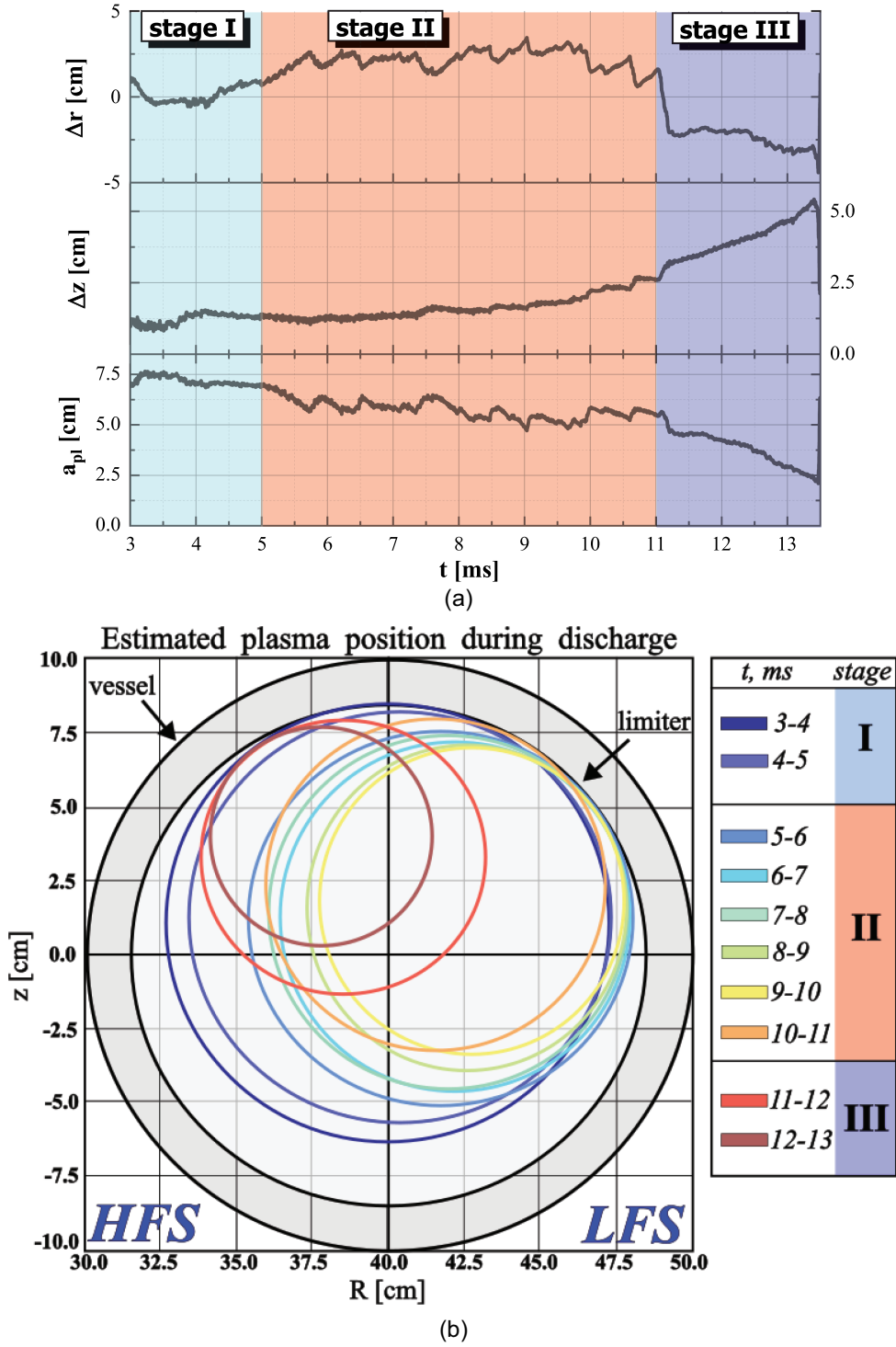$$\lambda = \frac{a_{pl}}{R_{pl}}\left(1 + \frac{\ell_i}{2} + \beta_{pol}\right) \quad ,$$

where

⊗ANS

Fig. 5. Evolution of the plasma position and plasma radius during typical plasma discharge #36598. (a) Time traces of $\Delta r$, $\Delta z$, and $a_{pl}$ according to Eqs. (2), (3), and (4). (b) Plasma last closed magnetic surface evolution with a step of 1 ms.

$R_{pl}$ = plasma major radius

$$\ell_i = \frac{\left\langle B_p^2 \right\rangle}{B_p^2(a_{pl})}$$

$$\beta_{pol} = \mu_0 \frac{\langle p \rangle}{\left\langle B_p^2 \right\rangle},$$
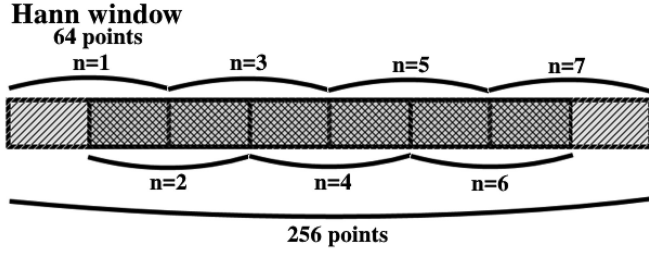
which take into account the toroidicity effect.

Fig. 6. Example of multiwindow fast Fourier transform technique.

The poloidal velocity of the $m = 2$ mode rotation was calculated. First of all, the shift of plasma column should be taken into account: Because of the different distance from the MC, the effective angle between neighbor coils is different. With knowledge of the plasma position (averaged for 1 ms), the effective angle between MCs, observable from the plasma column center, can be calculated; see Fig. 10.

Wave phase could be written as $\theta = \vec{k} \cdot \vec{r} - \omega t = n\varphi + m\vartheta - \omega t$. Cross phase is defined as $\Delta\theta = \vec{k} \cdot (\Delta\vec{r})$, in particular, toroidal cross phase $\Delta\theta_{tor} = k_{tor}\Delta l_{tor} = n\Delta\varphi$ and poloidal cross phase $\Delta\theta_{pol} = k_{pol}\Delta l_{pol} = m\Delta\vartheta$. Once the distance between MCs is known, the two-dimensional power spectrum $S\left(\vec{k}, f\right)$ between MC signals could be computed (for example, see Fig. 11). Information about wave-vector $\vec{k}$ at mode $m = 2$ frequency $f = (50 \pm 20)$ kHz allows one to calculate mode rotation velocity according to the following formulas:

$$\left|\vec{k}\right| = \sqrt{k^2_{tor} + k^2_{pol}}, \tag{11}$$

$$k_{pol} = \frac{\Delta\theta_{pol}}{a_{pl}\vartheta^*} \text{ and } k_{tor} = \frac{\Delta\theta_{tor}}{l_{tor}}, \tag{12}$$

and
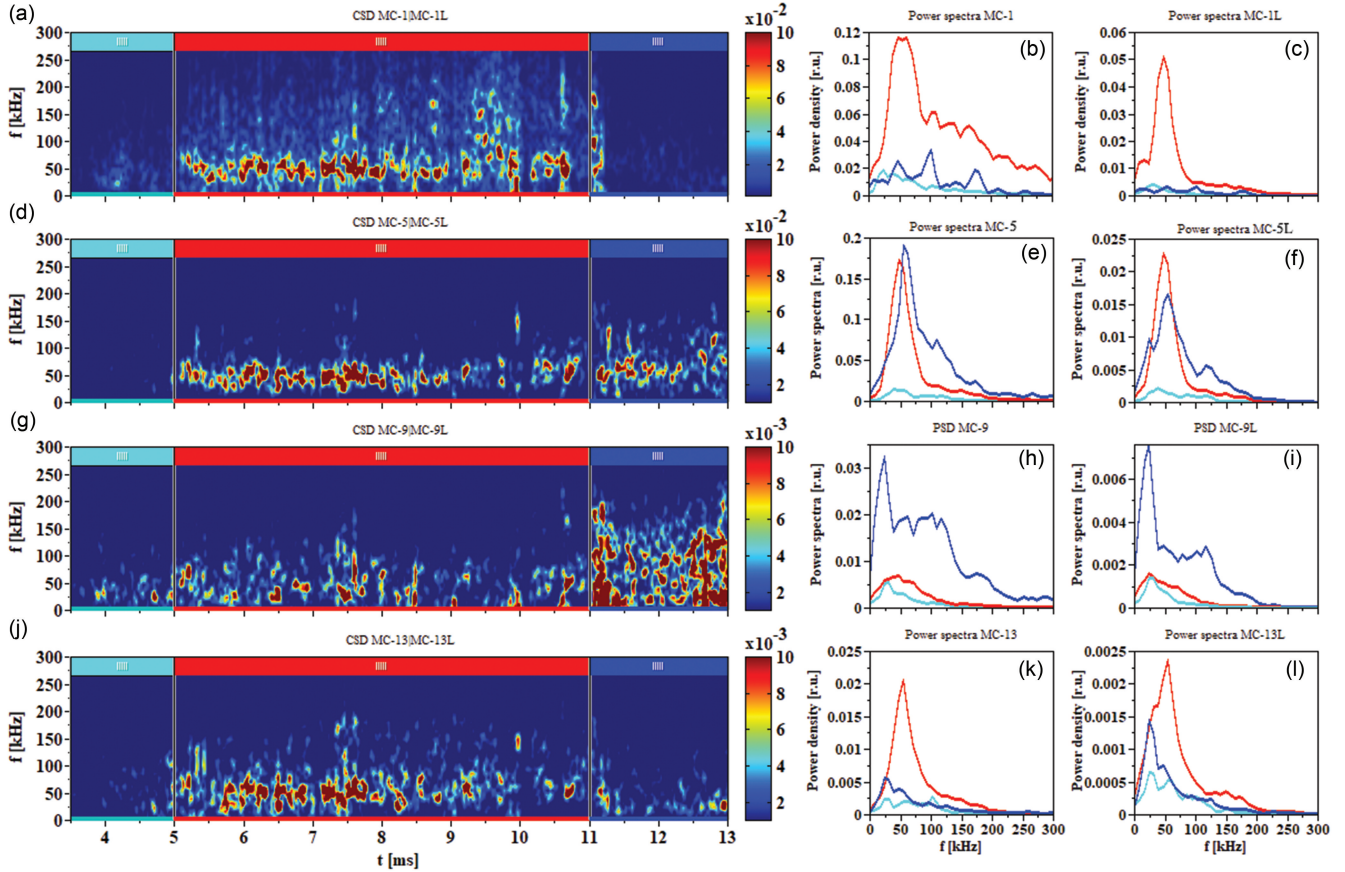


Fig. 7. (a), (d), (g), and (j) cross-spectral density spectrograms of MC-1|MC-1L, MC-5|MC-5L, MC-9|MC-9L, and MC-13|MC-13L. (b), (c), (e), (f), (h), (i), (k), and (l) The corresponding oscillation power spectra for three stages of the discharge; Stage I: light blue; Stage II: red; Stage III: dark blue.

⊗ANS

TABLE II

Time-Frequency Spatial Distribution of the Square Coherence Coefficient $\gamma_{ij}^2$ Between Magnetic Probes MC-1 Through MC-16
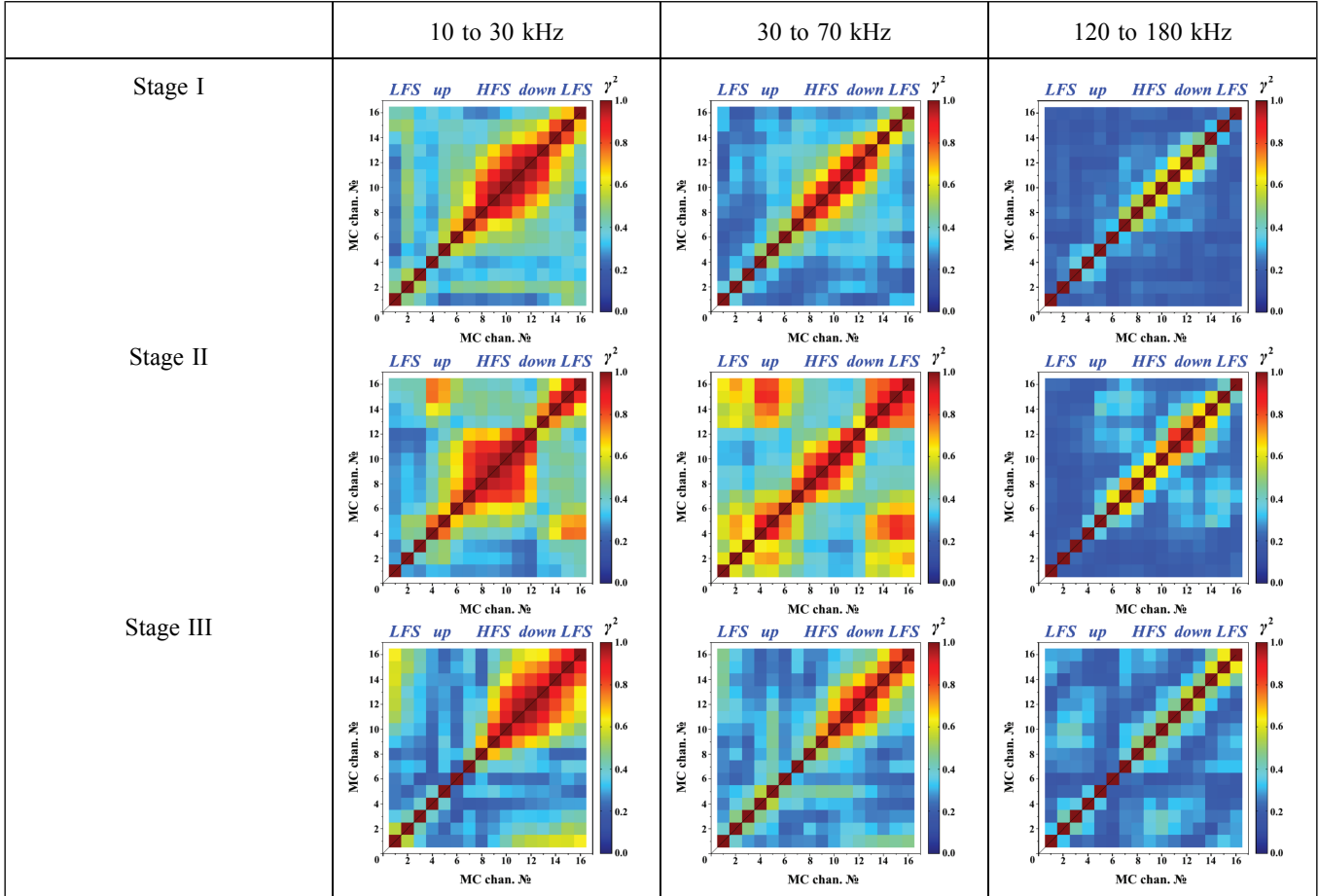


$$v_{pol} = \frac{\omega}{|\vec{k}|} \frac{k_{pol}}{|\vec{k}|} = 2\pi f \frac{k_{pol}}{k_{pol}^2 + k_{tor}^2}$$

and

$$v_{tor} = \frac{\omega}{|\vec{k}|} \frac{k_{tor}}{|\vec{k}|} = 2\pi f \frac{k_{tor}}{k_{pol}^2 + k_{tor}^2}. \tag{13}$$

As there are only four MCs located at the limiter cross sections, $k_{tor}$ and toroidal rotation velocity could be calculated at only four points: LFS (MC-1), up (MC-5), HFS (MC-9), and down (MC-13). Results for different times are presented in Table III. As can be seen, plasma shifting causes big errors in rotation calculation far from it (see HFS column). The power density of the signal provided by $m = 2$ becomes comparable with the power density of noise and broadband turbulence. That leads to velocity overestimation.

Toroidal mode number $n$ could not be estimated properly with only two cross sections with magnetic probes.

## IV. BROADBAND MAGNETIC TURBULENCE STUDIES

As is seen earlier, broadband magnetic turbulence dominates on MC signals at the HFS. In this case the right way is to study turbulence at the HFS. Cross-phase dependence of time can be associated with turbulence rotation as follows:

$$v_{rot} = \frac{\Delta l}{\Delta \tau} \; ,$$

where $\Delta \tau$ is a time delay between signals on the MC, which is obtained from the linear dependence of the cross phase on the frequency $\Delta\theta = -2\pi f \Delta\tau$, calculating the cross-phase spectrogram and extracting cross-phase spectra from it (notice that only the cross phase with coherence $\gamma^2 > \gamma_{conf}^2$ is taken into account); see Figs. 12 and 13.

Such spectra (see Fig. 14) were observed in works[25,29] for helium plasmas (see Fig. 15). The
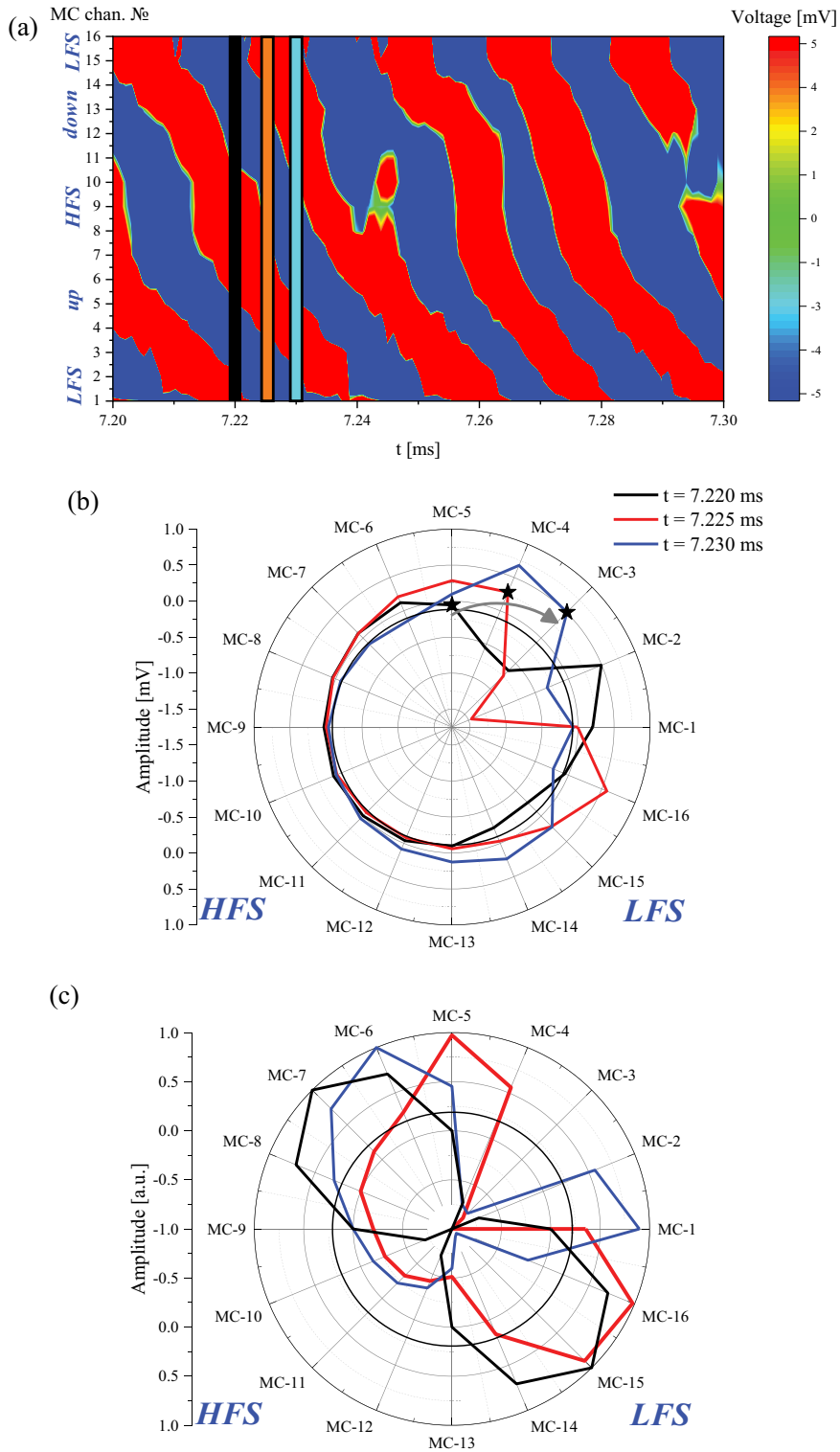
Fig. 8. (a) Time-channel contour plot (chronogram) of the magnetic perturbations. The time is shown horizontally, and the number of the magnetic probe is shown vertically. The color scale indicates the amplitude of oscillations (b). The spatial Fourier transform for times $t = 7.220$ ms, $t = 7.225$ ms, and $t = 7.230$ ms (marked in Fig. 8a with black, blue, and red lines). Arrow and stars mark the clockwise rotation direction. (c) Model of mode $m = 2$: black = pure mode with signal distribution $S = A\sin(2\theta)$, amplitude $A = 1$; blue = the same mode with account of toroidicity-induced disturbance of MC displacement. Red: Sine of experimental cross phase, which presents normalized oscillation with equal amplitude $A = 1$ for each MC. Taking into account dependency of $A$ on distance from MC, distribution as in (b) could be plotted.
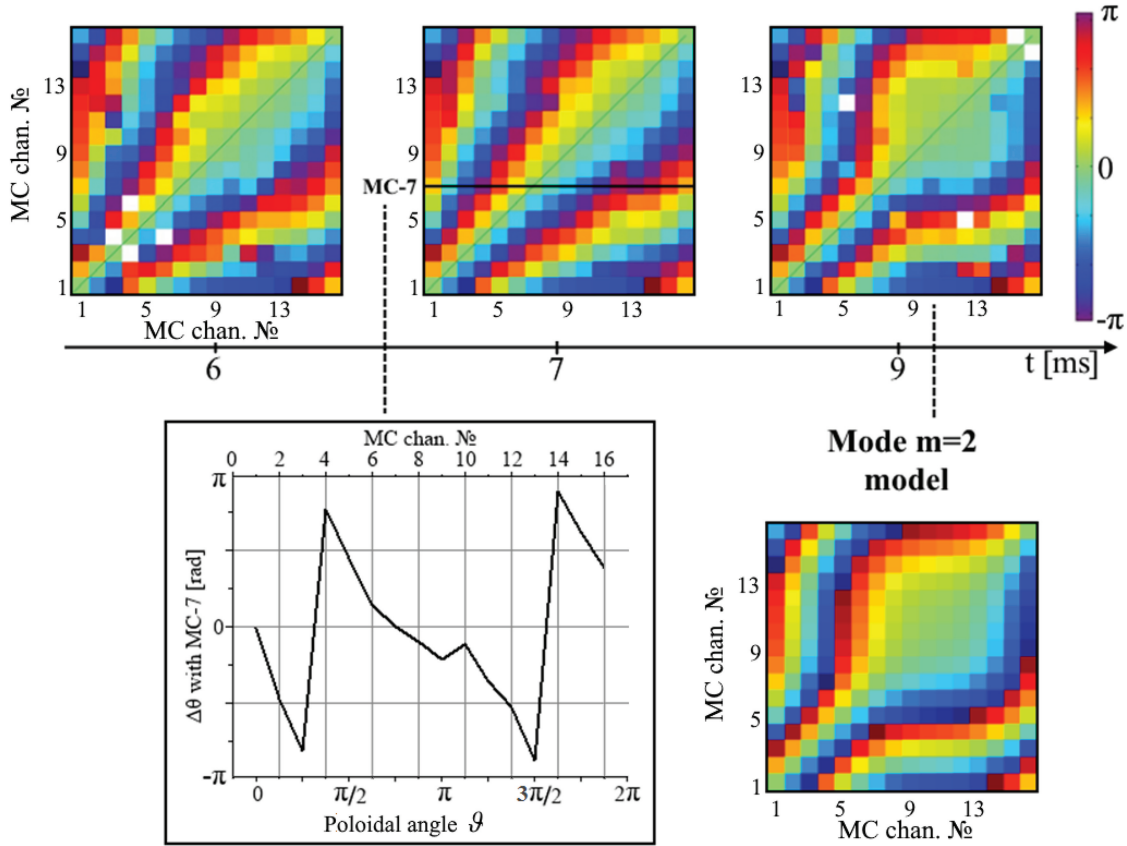
Fig. 9. (a) Temporal evolution of the MHD mode $m = 2$ during Stage II. (b) Spatial distribution of MC cross phase with MC-7 at $t = 7$ ms. (c) Numerical simulation of the cross phases between the MC signals for $m = 2$ with the transformation of poloidal angles $\vartheta^* = \vartheta - 0.9 \sin \vartheta$, done for the phase matrix at $t = 9$ ms.
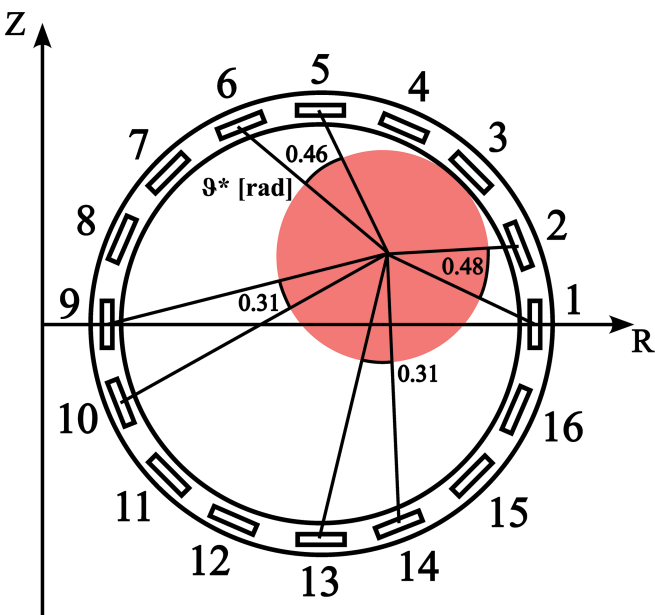


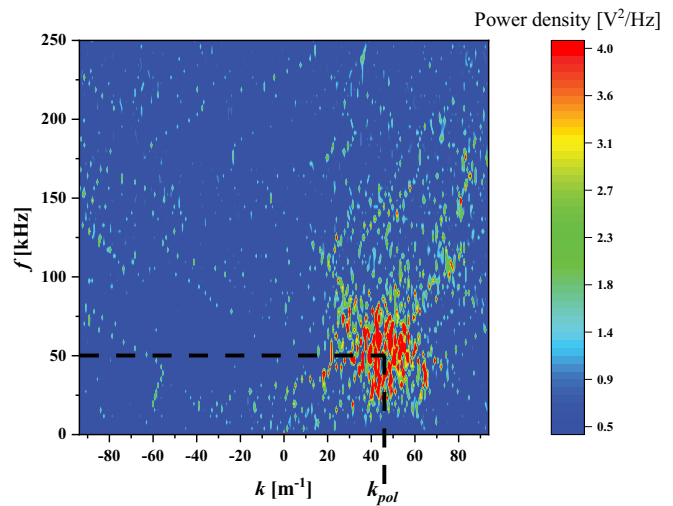Fig. 10. Effective angle $\vartheta^*$ between MCs at 7 to 8 ms.



Fig. 11. Two-dimensional power spectrum $S(k, f)$ of magnetic oscillations on probes MC-1|MC-2.

TABLE III

Poloidal and Toroidal Rotation Velocities for $m = 2$ Mode Calculated from
Toroidal and Poloidal Cross Phases of MC Signals at $f = (50 \pm 20)$ kHz.

| $v$ (km/s) | LFS (MC-1) | | Up (MC-5) | | HFS (MC-9) | | Down (MC-13) | |
|---|---|---|---|---|---|---|---|---|
| | $v_{tor}$ | $v_{pol}$ | $v_{tor}$ | $v_{pol}$ | $v_{tor}$ | $v_{pol}$ | $v_{tor}$ | $v_{pol}$ |
| $t = 6\text{--}7$ ms | 0.6 | 5.7 | 0.5 | 8.3 | 1.4 | 23.2 | 2.4 | 13.1 |
| $t = 7\text{--}8$ ms | 0.6 | 5.5 | 0.5 | 9.0 | 1.5 | 27.2 | 2.1 | 10.9 |
| $t = 8\text{--}9$ ms | 0.5 | 5.2 | 0.4 | 8.9 | 1.7 | 36.2 | 0.8 | 8.5 |
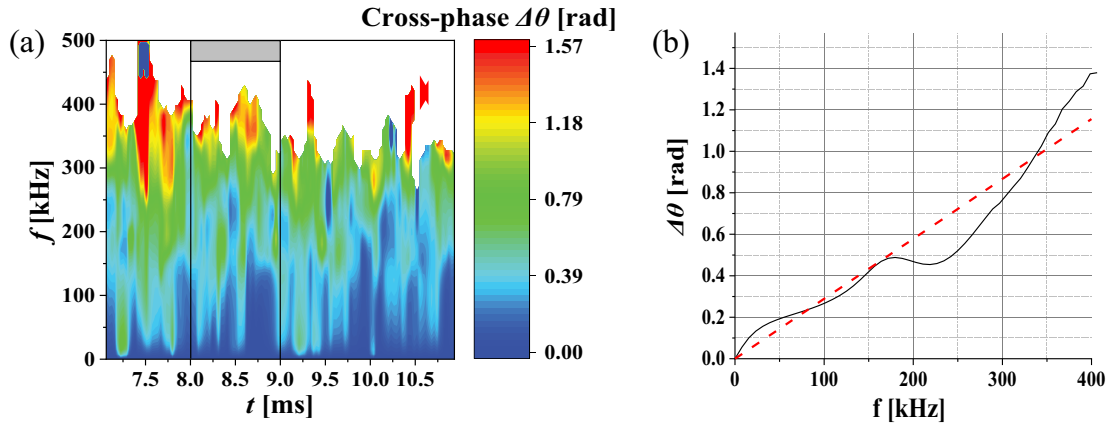


Fig. 12. Cross phase between MC-9|MC-9L, which represents toroidal propagation of broadband turbulence at the HFS, at the second stage of shot #36599.
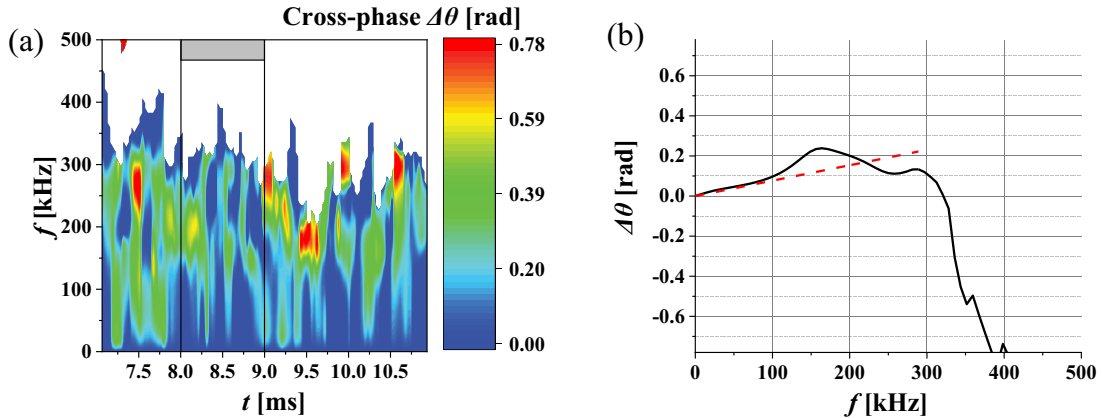


Fig. 13. Cross phase between MC-9|MC-10, which represents poloidal propagation of broadband turbulence at the HFS, at the second stage of shot #36599.

following turbulence rotation velocities in toroidal and poloidal directions were calculated: $v_{tor} = 13.3$ km/s and $v_{pol} = 3.6$ km/s. As could be seen, the velocities of the MHD mode rotation and broadband turbulence differ significantly.

## V. LONG-RANGE ELECTROSTATIC CORRELATIONS

Correlations between the floating potential signals of the LP and the DRP are observed. The distance between probes is 62.8 cm ($\pi/2$ in the toroidal direction). As can
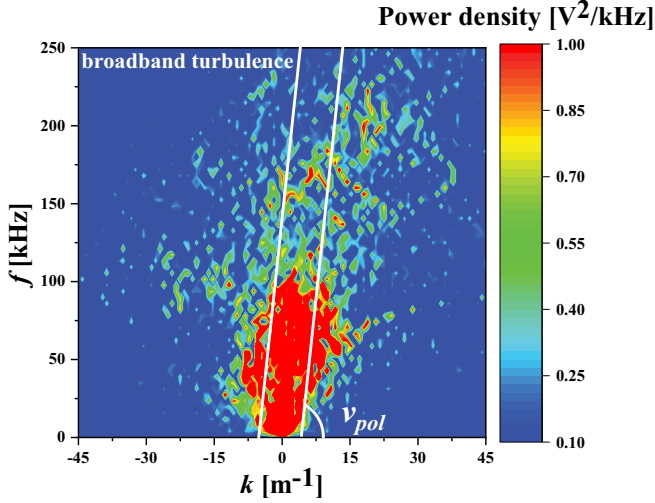
Fig. 14. Two-dimensional spectrum $S(k,f)$ of broadband oscillations on magnetic probes MC-8|MC-9, at the second stage of shot #36598.
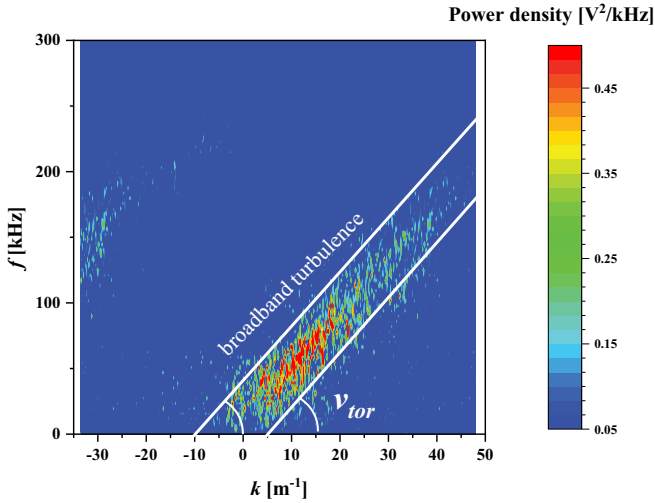


Fig. 15. Two-dimensional spectrum $S(k,f)$ of broadband oscillations on magnetic probes MC-L1|MC-L13, shot #33054, the second stage (He discharges).
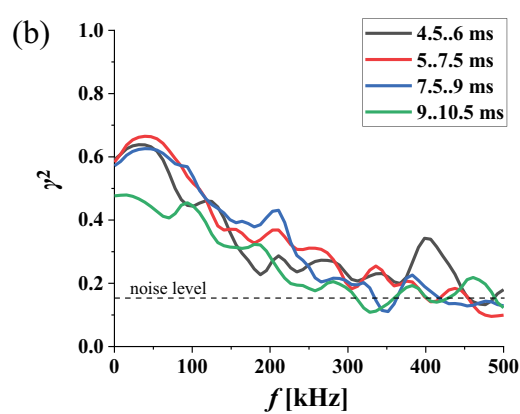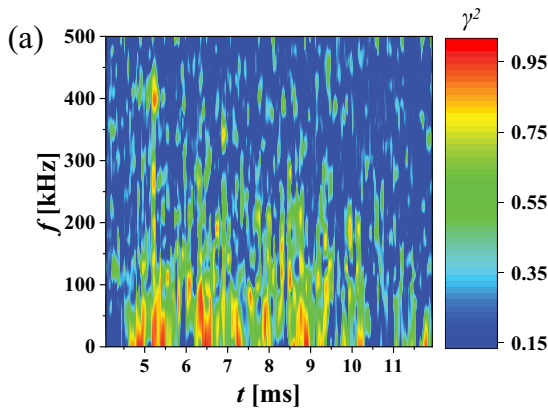
be seen in Fig. 16, during the discharge the broadband ($0 < f < 200$ kHz) structure seems not to change noticeably. At $f = 50$ kHz in Stage II of the discharge, a peak on the spectra of floating potential oscillation coherence is observed. But, unfortunately, it could not be seen in the coherence between magnetic and electric probes. Furthermore, the toroidal or poloidal number could not be calculated due to the location and number of the electric probes.

Measuring the cross phase between the LP and DRP-L1 (see Figs. 17a and 17b), it is possible to estimate the toroidal rotation velocity of electrostatic turbulence $v_{tor} \approx 7.4$ km/s.

An interesting fact is that despite the same frequency range and observation time of highly coherent magnetic oscillations and highly coherent electrostatic oscillations, they do not show any cross coherence among themselves; see Figs. 18a and 18b.

## VI. CONCLUSION

During student remote experiments in the GOLEM tokamak, MHD mode $f = 50$ kHz with poloidal number $m = 2$ has been observed in hydrogen plasmas. The mode has poloidal rotation velocity $v_{pol}^{m=2} = 6$ km/s.

Both broadband magnetic turbulence ($0 < f < 250$ kHz) and broadband electrostatic turbulence ($0 < f < 200$ kHz) indicate the features of toroidal plasma rotation. Both magnetic and electrostatic turbulences rotate in the cocurrent direction, but with different velocities: $v_{tor}^{mag} \approx 13$ km/s and $v_{tor}^{el} \approx 7$ km/s. The magnetic and electrostatic turbulence do not show the cross coherence indicative of their different origins and nature.



Fig. 16. Coherence spectrogram (a) and spectra of coherence averaged in 1.5-ms time windows (b) between floating potential measured by DRP and LP at the second stage of shot #36596. Color bar starts almost at the noise level 0.15.
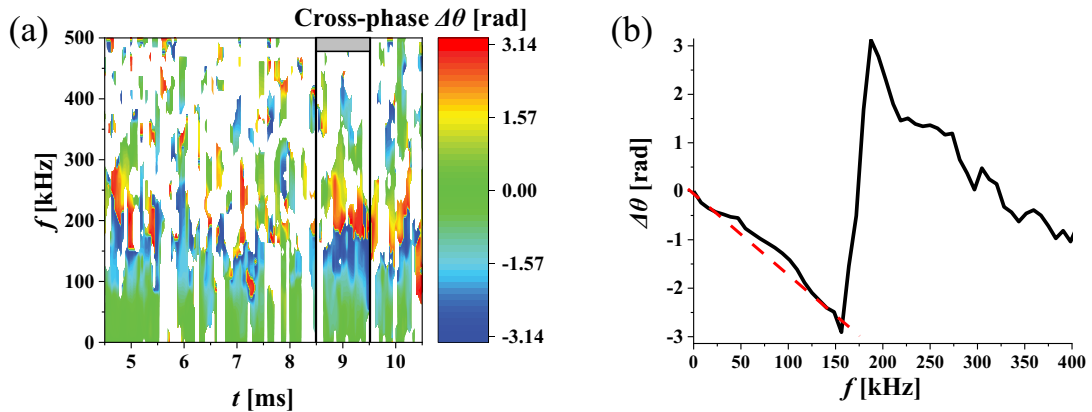
Fig. 17. (a) Spectrogram of the cross phase between floating potential measured by DRP-L1 and LP and (b) spectrum at the second stage of shot #36596.
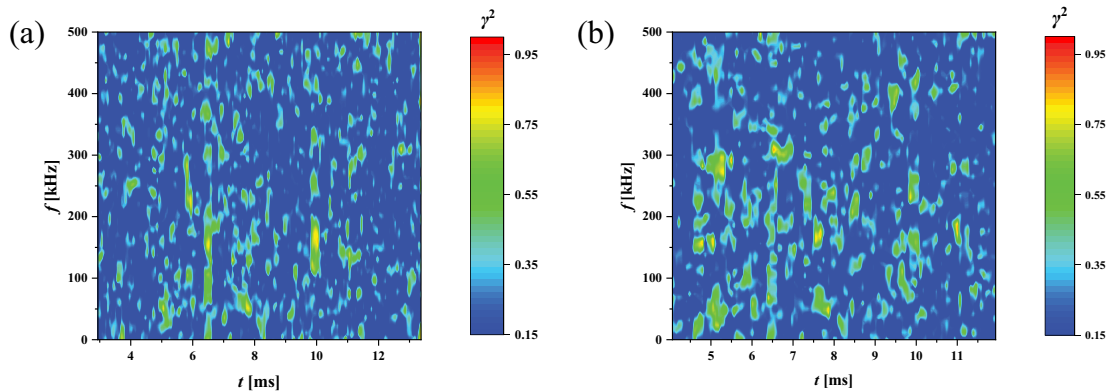


Fig. 18. (a) Cross coherence between magnetic oscillations MC-5 and floating potential measured by DRP-L1 and (b) cross coherence between magnetic oscillations MC-5 and floating potential measured by LP in shot #36597.

## Disclosure Statement

No potential conflict of interest was reported by the author(s).

## Data Availability

Datasets analyzed during the current study are available on the GOLEM web site at https://golem.fjfi.cvut.cz/shots/0.

## ORCID

G. Sarancha http://orcid.org/0000-0003-2723-5419
Ya. Ammosov http://orcid.org/0000-0001-9895-562X
A. Balashov http://orcid.org/0000-0001-5742-0768
O. Krokhalev http://orcid.org/0000-0002-4693-7590
A. Melnikov http://orcid.org/0000-0001-6878-7493
V. Svoboda http://orcid.org/0000-0003-1898-9120

## References

1. M. GRYAZNEVICH et al., "Results of Joint Experiments and Other IAEA Activities on Research Using Small Tokamaks," *Nucl. Fusion*, **49**, 10, 104026 (2009); 10.1088/0029-5515/49/10/104026.

2. M. GRYAZNEVICH et al., "Contribution of Joint Experiments on Small Tokamaks in the Framework of IAEA Coordinated Research Projects to Mainstream Fusion Research," *Plasma Sci. Technol.*, **22**, 5, 055102 (2020); 10.1088/2058-6272/ab6d4d.

3. V. SVOBODA et al., "Operational Domain in Hydrogen Plasmas on the GOLEM Tokamak," *J. Fusion Energy*, **38**, *2*, 253 (2019); 10.1007/s10894-019-00215-7.

4. V. SVOBODA et al., "Multi-Mode Remote Participation on the GOLEM Tokamak," *Fusion Eng. Des.*, **86**, *6*, 1310 (2011); 10.1016/j.fusengdes.2011.02.069.

5. O. GROVER et al., "Remote Operation of the GOLEM Tokamak for Fusion Education," *Fusion Eng. Des.*, **112**, 1038 (2016); 10.1016/j.fusengdes.2016.05.009.

6. P. MANAS et al., "The Confinement of Helium Tokamak Plasmas, Impact of Electron Heating, Turbulent Transport and Zonal Flows," *Nucl. Fusion*, **59**, *1*, 014002 (2019); 10.1088/1741-4326/aaeeb5.

7. R. E. WALTZ, R. L. DEWAR, and X. GARBET, "Theory and Simulation of Rotational Shear Stabilization of Turbulence," *Phys. Plasmas*, **5**, 1784 (1998); 10.1063/1.872847.

8. G. VAN OOST et al., "Multi-Machine Studies of the Role of Turbulence and Electric Fields in the Establishment of Improved Confinement in Tokamak Plasmas," *Plasma Phys. Control. Fusion*, **49**, *5A*, A29 (2007); 10.1088/0741-3335/49/5A/S03.

9. M. NAKATA et al., "Isotope Effects on Trapped-Electron-Mode Driven Turbulence and Zonal Flows in Helical and Tokamak Plasmas," *Phys. Rev. Lett.*, **118**, *16*, 1 (2017); 10.1103/PhysRevLett.118.165002.

10. G. R. MCKEE et al., "Observation and Characterization of Radially Sheared Zonal Flows in DIII-D," *Plasma Phys. Control. Fusion*, **45**, *12A*, A477 (2003); 10.1088/0741-3335/45/12A/031.

11. Y. XU et al., "Long-Distance Correlation and Zonal Flow Structures Induced by Mean E×B Shear Flows in the Biasing H-Mode at TEXTOR," *Phys. Plasmas*, **16**, *11*, 110704 (2009); 10.1063/1.3265367.

12. A. FUJISAWA, "Review of Plasma Turbulence Experiments," *Proc. Japan Acad. Ser. B*, **97**, *3*, 103 (2021); 10.2183/pjab.97.006.

13. P. DEVYNCK et al., "Dynamics of Turbulent Transport in the Scrape-Off Layer of the CASTOR Tokamak," *Phys. Plasmas*, **13**, *10*, 102505 (2006); 10.1063/1.2359721.

14. A. V. MELNIKOV et al., "Investigation of Geodesic Acoustic Mode Oscillations in the T-10 Tokamak," *Plasma Phys. Control. Fusion*, **48**, *4*, S87 (2006); 10.1088/0741-3335/48/4/S07.

15. J. SEIDL et al., "Electromagnetic Characteristics of Geodesic Acoustic Mode in the COMPASS Tokamak," *Nucl. Fusion*, **57**, *12*, 126048 (2017); 10.1088/1741-4326/aa897e.

16. A. KRÄMER-FLECKEN et al., "Investigation of Geodesic Acoustic Modes and Related Zonal Flows at TEXTOR," *Plasma Phys. Control. Fusion*, **51**, *1*, 015001 (2009); 10.1088/0741-3335/51/1/015001.

17. G. D. CONWAY, A. I. SMOLYAKOV, and T. IDO, "Geodesic Acoustic Modes in Magnetic Confinement Devices," *Nucl. Fusion*, **62**, *1* (2022); 10.1088/1741-4326/ac0dd1.

18. D. BASU et al., "Geodesic Acoustic Mode (GAM) Like Oscillations and RMP Effect in the STOR-M Tokamak," *Nucl. Fusion*, **58**, *2*, 024001 (2018); 10.1088/1741-4326/aa9a4f/meta.

19. G. A. SARANCHA et al., "Identification of Zonal Flows and Their Spatial Distribution in the TJ-II Stellarator Plasmas," *JETP Lett.*, **116**, *2*.

20. A. V. MELNIKOV et al., "Heavy Ion Beam Probing—A Tool to Study Geodesic Acoustic Modes and Alfven Eigenmodes in the T-10 Tokamak and TJ-II Stellarator," *Probl. At. Sci. Technol.*, **107**, *1*, 237 (2017).

21. V. N. ZENIN et al., "Plasma Potential Correlations Between Heavy Ion Beam Probe and Langmuir Probe on the T-10 Tokamak," *Probl. At. Sci. Technol.*, **118**, *6*, 321 (2018).

22. S. V. MIRNOV, "A Probe Method for Measuring the Displacement of the Current Channel in Cylindrical and Toroidal Discharge Vessels," *J. Nucl. Energy Part C*, **7**, *3*, 325 (1965); 10.1088/0368-3281/7/3/112.

23. D. E. SMITH, E. J. POWERS, and G. S. CALDWELL, "Fast-Fourier-Transform Spectral-Analysis Techniques as a Plasma Fluctuation Diagnostic Tool," *IEEE Trans. Plasma Sci.*, **2**, *4*, 261 (1974); 10.1109/TPS.1974.4316849.

24. R. O. R. Y. THOMPSON, "Coherence Significance Levels," *J. Atmospheric Sci.*, **36**, *10*, 2020 (1979); 10.1175/1520-0469(1979)036<2020:CSL>2.0.CO;2.

25. G. A. SARANCHA et al., "Magnetic Turbulence and Long-Range Correlation Studies in the GOLEM Tokamak," *J. Phys. Conf. Ser.*, **2055**, *1*, 012003 (2021); 10.1088/1742-6596/2055/1/012003.

26. A. V. MELNIKOV et al., "Quasicoherent Modes in the COMPASS Tokamak," *Plasma Phys. Control. Fusion*, **57**, *6*, 065006 (2015); 10.1088/0741-3335/57/6/065006.

27. V. G. MEREZHKIN, "Structure of Magnetic Field Perturbations During the Development of Disruption Instability in the Tokamak-6 Vessel," I. V. Kurchatov Institute of Atomic Energy (1977) (in Russian).

28. A. M. KAKURIN and I. I. ORLOVSKY, "Identification of the Structure of Large-Scale MHD Perturbations in a Tokamak from Mirnov Signals," *Plasma Phys. Rep.*, **29**, *10*, 826 (2003); 10.1134/1.1618888.

29. G. A. SARANCHA et al., "Hydrogen and Helium Discharges in the GOLEM Tokamak," *Probl. At. Sci. Technol. Ser. Thermonucl. Fus.*, **44**, *4*, 92 (2021); 10.21517/0202-3822-2021-44-4-92-110.

30. L. G. ELISEEV, "T-10 HIBP Signal Viewer," Patent RU 2015617233 (2015).